Tribol Lett (2016) 64:40
DOI 10.1007/s11249-016-0775-7

ORIGINAL PAPER

Airborne Wear Particles Generated from Conductor Rail and Collector Shoe Contact: Influence of Sliding Velocity and Particle Size

Yingying Cha[1] · Yolanda Hedberg[2,3] · Nanxuan Mei[2] · Ulf Olofsson[1]

Received: 30 August 2016 / Accepted: 14 October 2016 / Published online: 28 October 2016

Abstract The mechanical wear of train components is one of the main sources of airborne particles in subway air. A certain contribution is suspected to derive from third-rail systems due to the sliding of two metallic surfaces between conductor rail and collector shoe during operation. In this study, a pin-on-disc apparatus was used to simulate the friction between such two sliding partners (shoe-to-rail). Airborne particles generated from the sliding contact were measured by particle counters (a fast mobility particle sizer spectrometer and an optical particle sizer) and were collected by an electrical low-pressure impactor for physical and chemical analysis. Interface temperature for each test was measured by a thermocouple. The influence of sliding velocity and temperature on particulate number concentration, size distribution, and chemical composition was investigated. Atomic absorption spectroscopy, cyclic voltammetry, and energy-dispersive spectroscopy measurements were carried out to determine the chemical compositions. Results show that increasing sliding velocity results in a higher temperature at the frictional interface and a higher concentration of ultrafine particles. The ratio of manganese to iron surface oxides increased strongly with smaller particle size. A copper compound was observed in some particle samples, probably gerhardite ($Cu_2NO_3(OH)_3$) formed due to high temperature.

Keywords Sliding wear · Third-rail tribology · Particle emissions · Airborne wear particle · Oxidative wear

1 Introduction

Airborne particles in subway environments are incrementally attracting people's attention due to the high particle concentrations and their potential adverse effects on humans' health, especially if one is long-term exposed to those environments [1]. The levels of particulate matter (PM) concentrations in subway environments have been reported to exceed the limit value (i.e. 28 μg/m^3 for annual average PM10, and 17 μg/m^3 for annual average PM2.5) set by the EU in many cities, such as Naples, Barcelona, Los Angeles, Seoul, Prague, Paris, Stockholm [2–7]. A number of sources are considered to contribute to such high levels, such as wear of train components, re-suspended dust, and particles that transfer from ambient air. A third-rail system is commonly used for providing electric power to railway and subway trains. In Stockholm and in many other cities, all of the metro trains are electrically powered by the contact of third rail and collector shoe. Subway particles in Stockholm were primarily nano-sized, contained metals, carbon, and organic compounds, with a potentially genotoxic effect [8–10]. According to previous studies [11, 12], the sliding friction of conductor rail and collector shoe would result in abundant iron- and copper-

Electronic supplementary material The online version of this article (doi:10.1007/s11249-016-0775-7) contains supplementary material, which is available to authorized users.

✉ Yingying Cha
yingcha@kth.se

[1] Department of Machine Design, School of Industrial Engineering and Management, KTH Royal Institute of Technology, Brinellvägen 83, 10044 Stockholm, Sweden

[2] Division of Surface and Corrosion Science, Department of Chemistry, School of Chemical Science and Engineering, KTH Royal Institute of Technology, Drottning Kristinas väg 51, 10044 Stockholm, Sweden

[3] Unit of Work Environment Toxicology, Institute of Environmental Medicine, Karolinska Institutet, Nobels väg 13, 17177 Stockholm, Sweden

containing particles, where copper is an abundant component.

Experimental tests have indicated that wear debris released from third-rail and shoe material contains a certain amount of iron, copper, chromium, and their oxides [13, 14]. Material volume loss caused by electrical arc erosion is reported to be much larger than those caused by mechanical wear [13]. When sliding along third rail, the shoe vibrates and moves in and out of contact. This affects the generation of arc discharges and further influences the wear mechanisms [15]. Temperature is also suggested to be a key factor that has significant effect on particulate emissions. The increased frictional heat between shoe–rail sliding contact is believed to be an important factor for affecting the wear mechanism [14]. The significant rise in wear of the frictional pair at high temperature is attributed to accelerated oxidation [16, 17]. Another different opinion is that the rate of wear of the frictional metal pair reduces as the temperature increases due to the formation of oxide protective layers. An experimental investigation on the friction of high strength steel concludes that at high temperature (above 300 °C), the formation of a stable-load oxide bearing bed and eventually a glaze-layer leads to the significant reduction in wear [18]. The wear rate is determined by the oxidation rate for the test of the sliding of hard steel in dry air [19]. It reveals that above 300 °C the wear decreases with increasing temperature since the surfaces develop relatively thick oxide layers and polished patches which are suggested to be compacted oxide wear debris. The wear debris from the high carbon tool steel at these high temperatures is Fe_3O_4 which is adherent and wear protective. It is suggested that the temperature has an effect on the wear protective oxide layer particularly above 250 °C [20]. One of the main reasons is that the oxidation rates become faster at higher temperatures, which can promote the development of compact and adherent wear protective oxide layers. The diameter size of oxide particles is believed to affect the wear rate of rubbing steel as well. When supplying Fe_2O_3 oxide particles to rubbing steel surfaces, it is demonstrated that finer particles (nanometre-sized) are easily sintered on the wear surface thereby inducing rapid transition to mild wear due to the formation of the wear-protective tribofilm on the surfaces, while no severe-mild wear transition is observed when adding larger particles on the rubbing surfaces but an increase in the wear rate of the contact on the contrary [21, 22].

Some previous studies have been performed to investigate the effect of temperature on the emission of airborne particles from fictional metal pairs. It is concluded from a study of low-metallic brake material [23] that at temperatures above 300 °C, an elevated number of ultrafine wear particles is generated via evaporation and condensation wear mechanisms of carbonaceous components, while particles larger than 500 nm are generated at a lower temperature. One study of dry sliding frictional tests between wheel and rail samples was conducted by Sundh and Olofsson [17]. It shows that a large number of small particles in the ultrafine size range are observed at elevated temperatures as the sliding velocity increased. However, studies on particle emissions from mechanical friction of rail to shoe are scarce.

To investigate the particulate emission from the sliding contact between collector shoe and conductor rail, a series of pin-on-disc tests were carried out. The focus of the investigation was the dependence of particulate concentration, size distribution, and chemical composition on sliding velocity. The effect of temperature in dependence of sliding velocity was studied in addition, as temperature is an important influencing factor on the wear mechanism [14, 19]. Scanning electron microscope (SEM) equipped with energy-dispersive spectroscopy (EDS), atomic absorption spectroscopy (AAS), and cyclic voltammetry (CV) measurements were applied to study the morphology, elemental and chemical composition of the particles in dependence of their size, using 14 different size fractions between <17 nm and <10 μm, collected by an electrical low-pressure impactor (ELPI+). This study enables an insight into wear mechanisms, and wear particle composition dependent on particle size, of relevance for wear particles in subway systems using a third-rail power supply.

2 Experimental Methodology

2.1 Pin-on-Disc Apparatus with Particle Sampling and Collecting Instruments

Laboratory experiments were carried out by a pin-on-disc tribometer, which was the same set-up used previously by Olofsson et al. [24–26]. The schematic of the machine structure is presented in Fig. 1. The pin-on-disc machine (H) was placed inside a closed chamber (G). It was mounted with a deadweight-loaded pin (I) and a horizontal rotating disc (M). Hepa-filtered air (A) was brought into the sealed chamber, with an airflow velocity of 0.44 m/s. Airborne wear particles generated from the sliding contact between pin and disc were measured by particle measurement instruments (a FMPS and an OPS, see below for description) and were simultaneously collected by an ELPI+. These instruments were connected to the air outlet (J). During all tests, the temperature of the contact interface was monitored by a thermocouple (T) with a sensor wire inserting into the pin specimen with one millimetre away from the contact interface. In order to reduce heat loss

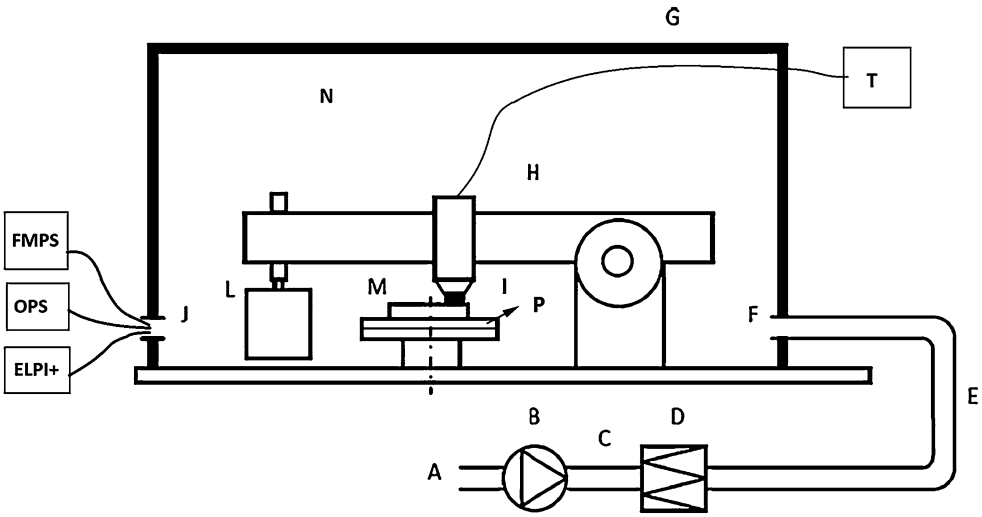

Fig. 1 Schematic structure of the pin-on-disc set-up: (*A*) room air, (*B*) fan, (*C*) flow rate measurement, (*D*) filter, (*E*) flexible tube, (*F*) inlet for clean air, (*G*) closed chamber, (*H*) pin-on-disc machine, (*I*) pin, (*J*) outlet and measurement points, (*L*) dead weight, (*M*) rotating disc, (*N*) air inside the chamber, (*P*) insulator plate, and (*T*) thermocouple

transferring into the disc holder, an insulator plate (P) was used. A more detailed working principle of this apparatus was introduced already in previous studies [24–26]. A major limitation of this set-up is the lack of current flowing through the specimens. This has been shown to affect the temperature in the interface and consequently wear mechanisms [13, 27, 28]. In addition, there is discontinuous contact between the third rail and the shoe due to the vibrations and impactions as the shoe reengages with the rail after dead zones. This differs from the laboratory tests in this study, where the sliding contact is continuous without significant vibrations.

An optical particle sizer (OPS, Model 3330) is used to measure particle number concentration by using the single particle counting technology. Particle mass concentration can also be measured based on a unit density (1 g/cm^3). In this case, the density of a particle refers to effective density that includes porosity and shape. The allowable operational temperature and humidity are 0–45 °C and 0–96 % RH, non-condensing, respectively. The time resolution was set to be one second and sampling flow rate was 1.0 L/min, with ±5 % accuracy. It is used to measure particles in the size range of 0.3–10 μm with up to 16 separated channels. With it, partly fine (100 nm–2.5 μm) and coarse (2.5–10 μm) particles can be measured, but not ultrafine (<100 nm). For ultrafine and partly fine particles, a fast mobility particle sizer spectrometer (FMPS, Model 3091) was used. It is able to measure particle concentration and size distribution of ultrafine and partly fine particles in the mobility diameter size range of 6.04–523.3 nm. By using the FMPS, particulate matters can be counted by their number concentrations with a total of 32 size-separated channels. The time resolution was one second. The sampling flow rate was set to 10 L/min and the particle density 1 g/cm^3 for mass concentration measurement. Moreover, an ELPI+^{TM} (electrical low-pressure impactor) was used to collect particles on size-separated stages. It composes 15 stages and enables the collection of airborne particles (with an aerodynamic diameter size range of between 6 nm and 10 μm) on 14 sized filters (Table 1). In order to prevent particle bounce and blow off, filter substrates are usually recommended to be coated with DS-515 grease spray before impactor measurements. The allowable operational temperature and humidity are 10–35 °C and 0–90 % RH, non-condensing, respectively. The sampling flow rate was 10 L/min, and the data acquisition rate was set to be 10 Hz.

2.2 Materials and Parameters

Conductor rail and collector shoe samples were cut from commercial third-rail and shoe materials, which are used ones that have been in service in the Stockholm metro system. Their elemental compositions (metals only) were determined by inductively coupled plasma (ICP), as results presented in Table 2. The collector shoe was made into pin specimens with 10 mm in diameter and 15 mm in thickness. In order to monitor the friction temperature during tests, all pins were manufactured with a central hole (1 mm in diameter and 1 mm distance away from the contact interface) to insert the sensor wire of a thermocouple. The

Table 1 Specification of ELPI+^{TM} channels

Filter number	Da (μm)	Filter number	Da (μm)
1	0.017	8	0.64
2	0.03	9	1.0
3	0.06	10	1.6
4	0.108	11	2.5
5	0.17	12	4.4
6	0.26	13	6.8
7	0.4	14	10

Table 2 Elemental metal composition of the conductor rail and collector shoe material (wt%)

Element	Third rail	Shoe C20
Fe	99.8	97.7
Cu	0.01	0.757
Mn	0.169	0.284
Si	0.035	1.02
Cr	0.02	0.025
Ni	0.033	0.022
K	<0.005	0.037
Al	0.035	0.019
Mo	0.001	0.003
As	<0.005	0.006
Sn	<0.001	0.002
Zn	<0.0005	0.002

conductor rail was manufactured into disc specimens with 100 mm in diameter and 15 mm in thickness. An electrical balance with a resolution of ±0.00005 g was used to determine the mass of the pins, and another electrical balance with a resolution of ±0.0005 g was used to measure the mass of the discs before and after all the tests. All the samples were cleaned ultrasonically by isopropanol in an ultrasonic bath for 30 min and were dried before weighing.

For microhardness measurements of the third-rail and shoe materials, an extra pin (shoe) and a cylindrical sample (15 mm in diameter) cut from the third rail were wet-polished. The Vickers hardness of each sample was measured by a Matsuzawa microhardness tester (MXT-α1) equipped with a pyramidal diamond indenter with a load of 1000 g for 20 s. Four different points were tested for each sample. The indentations were assessed by an optical microscope (Olympus), and the HV values (in HV) were calculated by digital image processing and analysis software (Leica QWin). Those values in HV were converted to values in GPa according to the expression $Hv = \frac{1.854F}{d^2}$, where F is force applied (in kgf) and d is the average indentation diagonal (in mm); hence, $1Hv = 9.807$ MPa $= 0.009807$ GPa. The Vickers hardness (average of the 4 values for 4 points) of third-rail material is 1.15 and 2.48 GPa for the shoe.

2.3 Experimental Procedure

Four pairs of test were conducted with four different rotating speeds applied to correspond to four different sliding velocities, as shown in Table 3. Two tests were performed to simulate a variable velocity (from 0 to 7.2 m/s) with a linear function of velocity versus sliding time, while the other tests were run at a constant velocity, Table 3. The varying velocity consisted of three intervals, i.e. constant acceleration (0.02 m/s^2, last for 360 s), constant velocity (10 s), and constant deceleration (0.12 m/s^2, last for 60 s). Duplicate tests of a constant velocity had similar test conditions, except test duration and collecting particle filters inside the ELPI+. A constant normal load (41.8 N) between a pin and a disc was applied for all tests. That corresponds to a pressure of 0.5 MPa. According to a technical report by Schunk, the working pressure of third-rail contact is between 0.4 and 0.8 MPa [29]. The airflow velocity at inlet was controlled to 0.44 m/s at the beginning of each test. Test durations were controlled to a sliding distance of 4320 m for test 1.2a, test 3.6a, and test 6a. An exceptional value (2880 m) for test 1.2a was due to a wrong setting of the thermocouple. Longer durations for test 3.6b and test 6b were aimed to collect enough particles for post chemical analysis. Test 3.6c and test 6c were repeated tests for test 3.6a and test 6a, respectively, to obtain a higher mass of particles for chemical analysis and that the chemical analysis is based on the particles from those tests. Particles collected from test 1.2a, test 3.6b, and test 6b were chemically analysed by atomic absorption spectroscopy (AAS). Particles collected from test 1.2b, test 3.6c, and test 6c were for cyclic voltammetry measurements. Before each test, the chamber was cleaned by a vacuum cleaner firstly and then was further cleaned by paper wetted by isopropanol to guarantee a clean environment. The average room temperature and humidity was 20 (±2) °C and 24 % RH, respectively. Particulate concentration, size distribution, friction force, and interface temperature were measured simultaneously for each test.

2.4 Wear Surface Investigation Using Microscopic Techniques

After the wear tests, all pin and disc specimens were firstly observed for their worn surface using an optical microscope (Olympus BH2). Some of them were further analysed by a scanning electron microscope (SEM, Hitachi S-3700N), using both the secondary electron and backscattered electron mode, combined with an energy-dispersive X-ray microanalysis system (EDS).

2.4.1 Digestion of Filter Samples

0.6 mL 25 % HCl (p.a. grade), 0.6 mL 65 % HNO_3 (p.a., normapur grade), and 4.8 mL ultrapure (18.2 MΩ cm, Millipore, Solna, Sweden) water were added to each polycarbonate filter with the collected wear particles in acid-cleaned centrifuge tubes. They were sonicated (in an ultrasonic bath) for 1 h and stored in this solution for 1 week prior to AAS analysis. This method has been validated by digesting and analysing iron powder of known mass, with a recovery of >85 %. Two blank samples

Table 3 Wear test parameters and particle collection filters

Test no.	Normal load (N)	Sliding velocity (m/s)	Sliding distance	Filter type
Test va/b	41.8	Varying from 0 to 7.2	430 (s)	Not collected
Test 1.2a/b	41.8	1.2	2880 (m)	PC/AG
Test 3.6a/b	41.8	3.6	4320/8640 (m)	AG/PC
Test 6a/b	41.8	6	4320/14,400 (m)	AG/PC
Test 3.6c	41.8	3.6	8640 (m)	AU
Test 6c	41.8	6	14,400 (m)	PC

PC: Polycarbonate

AG: Aluminium-greased

AU: Aluminium-ungreased

(unused polycarbonate filters without any particles) were prepared identically to determine the background concentration levels.

2.4.2 Atomic Absorption Spectroscopy

The total mass of iron (Fe), manganese (Mn), and copper (Cu) were determined by atomic absorption spectroscopy (AAS), either in the flame (for Fe and some samples of Cu and Mn) or the graphite furnace mode. Calibration standards with Fe concentrations of 10, 20, 50, and 100 µg/L, or of 0.5, 1, and 5 mg/L, or of 10, 30, and 60 mg/L were prepared using 1 % HNO_3 (p.a. grade for mg/L standards and puriss. p.a. grade for µg/L standards) to mimic the acidic condition of acidified solution samples for analysis and to hinder precipitation of metals. Several calibrations and modes (flame and graphite furnace) were necessary to analyse Fe concentrations in the samples accurately. 10, 30, and 100 µg/L calibration standards were used for the Cu and Mn graphite furnace (GF) analysis. Some copper samples were diluted 10 times to ensure their concentrations to be within the calibration range. Quality controls (in 1 % HNO_3) were performed every 5th to 7th sample (for each mode). If they deviated more than 10 % from their nominal concentrations, the analysis was repeated. One matrix modifier, magnesium nitrate, was used for the GF analysis of Fe, and two matrix modifiers, palladium nitrate and magnesium nitrate, were used for the GF analysis of Mn and Cu. The limits of detection, calculated as maximum blank values plus three times the highest standard deviation of the blanks, were 34 µg/L (Fe GF analysis), between 55 and 103 µg/L (Fe flame analysis), 2.3 µg/L (Cu, GF analysis), and 0.98 µg/L (Mn, GF analysis). The blank values were 32.6 µg/L Fe (GF), 2.0 µg/L Cu (GF), and 0.62 µg/L Mn (GF). All reported values are based on concentrations that are higher than their corresponding limits of detection. The mass on filter (µg) is calculated as follows:

$$\mathrm{Mass}(\mu g) = \left(\text{sample metal concentration}\left(\frac{\mu g}{L}\right) - \text{blank concentration}\left(\frac{\mu g}{L}\right)\right) * \text{volume}\left(0.006 L\right)$$

Results are furthermore normalized to the sliding distance (Table 3). The particle number for each size fraction is furthermore calculated based on the mass detected for Fe, Cu, and Mn for each size fraction. Given the density of Fe, the main element of the particles, of 7.874 g/cm^3, the total volume of each size fraction can be obtained. Spherical particles of the average size of each size fraction are assumed with a volume based on the diameter of each size fraction, for example 0.0085 µm ((0.017–0)/2 = 0.0085) for the first size fraction (Table 1). The total number of particles in each size fraction is hence the total volume divided by the single sphere volume, and this calculation was used:

$$\frac{\text{Particle number}}{\text{sliding distance(km)}} = \frac{\mathrm{Mass}(\mu g) * 10^{15}}{7.847 \frac{g}{cm^3} * \left(\frac{\text{particle diameter}(\mu m)}{2}\right)^3 * \frac{4}{3} * \pi * 10^9 * \text{sliding distance(km)}}$$

2.4.3 Cyclic Voltammetry

2.4.3.1 Using a Graphite Paste Electrode 100 mg graphite powder (natural, briquetting grade, 100 mesh, 99.9995 % (metal basis), UCP-1 grade, Ultra "F" grade, Lot no. 61200620, Alfa Aesar, Sweden) was mixed with the collected wear particles directly on the aluminium filters. This mixture was gently pressed and mixed with a pestle. A few drops of the electrolyte [8 M NaOH (pH ~ 13)] were added to obtain a paste. The paste was positioned into a small (Ø 1.9 cm, height 7.0 cm) glass container connected with a platinum wire to act as the working electrode. The counter electrode (a platinum wire wrapped around the reference electrode) and the reference electrode (Ag/AgCl sat. KCl) were positioned approximately 1 cm from the

graphite paste in the electrolyte. The system was, prior to the measurements, allowed to equilibrate before determining the open-circuit potential (OCP) for 300 s (or until the change of OCP was less than 1 μV/s). The potential was then swept cathodically (to more negative potentials) starting at the OCP at a rate of 0.0005 V/s towards a potential of approximately −1.4 V (vs. Ag/AgCl sat. KCl), after which the potential was swept anodically until a potential of approximately +0.2 V. Some measurements were performed in the other direction, that is, first oxidized to +0.2 V and then reduced to −1.4 V, after which they were oxidized until OCP, denoted "oxidation → reduction".

A high contamination from the aluminium filters was observed (from parallel tests on filters not containing any wear particles). Therefore, the tests were continued with a PIGE instead (following section) that is pressed onto the particles. The reason is that the aluminium filters are heavily scratched and damaged while preparing the graphite paste.

2.4.3.2 Using a Paraffine-Impregnated Graphite Electrode (PIGE) A PIGE (which did not show any peak without any particles attached to it, nor when pressed onto a particle-free filter) was used as the electrode in the same cell and under the same conditions as described above. The PIGE was heated with a lighter, to soften the paraffine, and afterwards pressed onto the aluminium or polycarbonate filters to pick up particles from the filter. One cyclic voltammogram was run for the following samples in Table 4.

Figure 2 illustrates the set-up of the electrochemical cell and measurement.

The program used to determine the peak areas was Origin 2015 64 Bit, function "Integrate". A linear base line was used, which introduced an error especially in the case of the oxidation peak at −1.1 V. Peaks close to 1 E-9 VA were close to the background noise. Reduction peaks can be hidden in the large H_2 evolution peak, especially for the Fe reduction peak at −1.3 V. They can also be hidden in the O_2 adsorption peak in the beginning of reduction.

Table 4 Cyclic voltammetry measurements

Test 1.2b (1.2 m/s)	Number 6 filter	Reduction → oxidation
	Number 8 filter	Reduction → oxidation
	Number 10 filter	Reduction → oxidation
	Number 11 filter	Oxidation → reduction
Test 3.6c (3.6 m/s)	Number 4 filter	Oxidation → reduction
	Number 5 filter	Reduction → oxidation
	Number 7 filter	Reduction → oxidation
	Number 10 filter	Oxidation → reduction
	Number 11 filter	Reduction → oxidation
Test 6a (6 m/s)	Number 7 filter	Reduction → oxidation
	Number 8 filter	Reduction → oxidation
	Number 10 filter	Reduction → oxidation
	Number 11 filter	Reduction → oxidation
Test 6c (6 m/s)	Number 4 filter	Reduction → oxidation
	Number 5 filter	Oxidation → reduction
	Number 9 filter	Oxidation → reduction
	Number 10 filter	Reduction → oxidation
	Number 11 filter	Reduction → oxidation
	Number 12 filter	Oxidation → reduction

2.4.4 SEM/EDS Test of Particles

Particles of test 1.2b (number 14), test 3.6a (number 10), test 6a (number 6), and test 6a (number 12) were investigated (at 4–6 different locations) with a tabletop scanning electron microscope (SEM) with backscattered electron analysis (Hitachi TM-1000) and energy-dispersive spectroscopy (EDS) to determine their main elements (light elements such as C, O, H, and N cannot be determined by

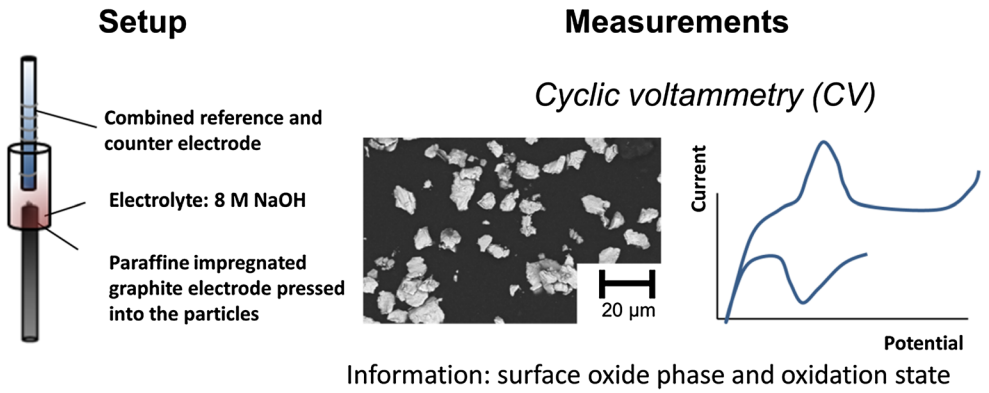

Fig. 2 Schematic overview of cyclic voltammetry on particles, a typical example of the wear particle morphology (SEM image, magnification ×1000) is also shown (number 14 filter of test 1.2b)

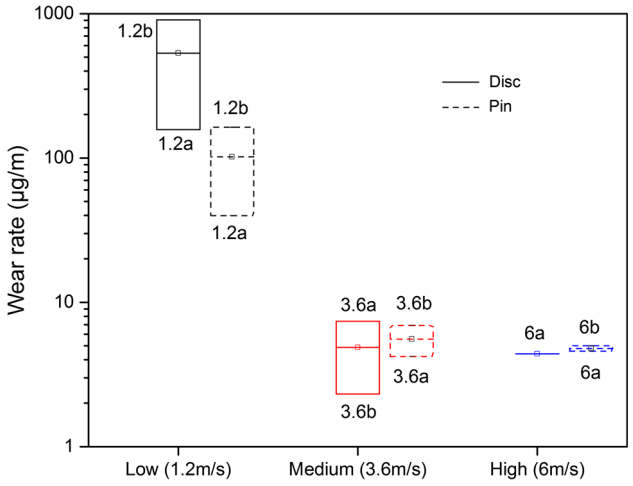

Fig. 3 Wear rate [total mass loss (µg) over the entire sliding distance (m)] of pins and discs for different sliding velocities, 1.2a/b, 3.6a/b, and 6a/b marking test 1.2a/b, test 3.6a/b, and test 6a/b. The *box* comprises values of parallel test (*upper* and *bottom line*). The *line* and the *square* inside the *boxes* represent the mean values

this instrument). The powders were fixed on carbon tape to avoid dispersion inside the instrument chamber and to assure appropriate conduction.

3 Results

3.1 Wear Rate and Friction Coefficient

Wear rate is calculated by the mass loss per unit distance, that is the difference of mass (µg) before and after test over the total sliding distance (m). The unit of wear rate is µg/m. Figure 3 shows the results for the cases with constant sliding velocities of 1.2, 3.6, and 6 m/s. It can be seen that the wear rates of both pin and disc with low velocity (1.2 m/s) are remarkably higher than those with a medium (3.6 m/s) and high velocity (6 m/s). For the latter two cases, the corresponding wear rate is similar. The wear rate of the disc for test 6b, which is negative, is not included. One reason for a negative wear rate is that a certain amount of particles is tightly attached to the surface and is hard to remove by ultrasonic cleaning.

Figure 4 shows average friction coefficients with standard errors for two parallel tests with three constant and one varying velocity. For varying velocity, the friction coefficient is unstable in the beginning of acceleration and in the deceleration periods. It decreases dramatically to around 0.4 when that velocity is around and above 3 m/s. With respect to the cases with constant velocities, it can be

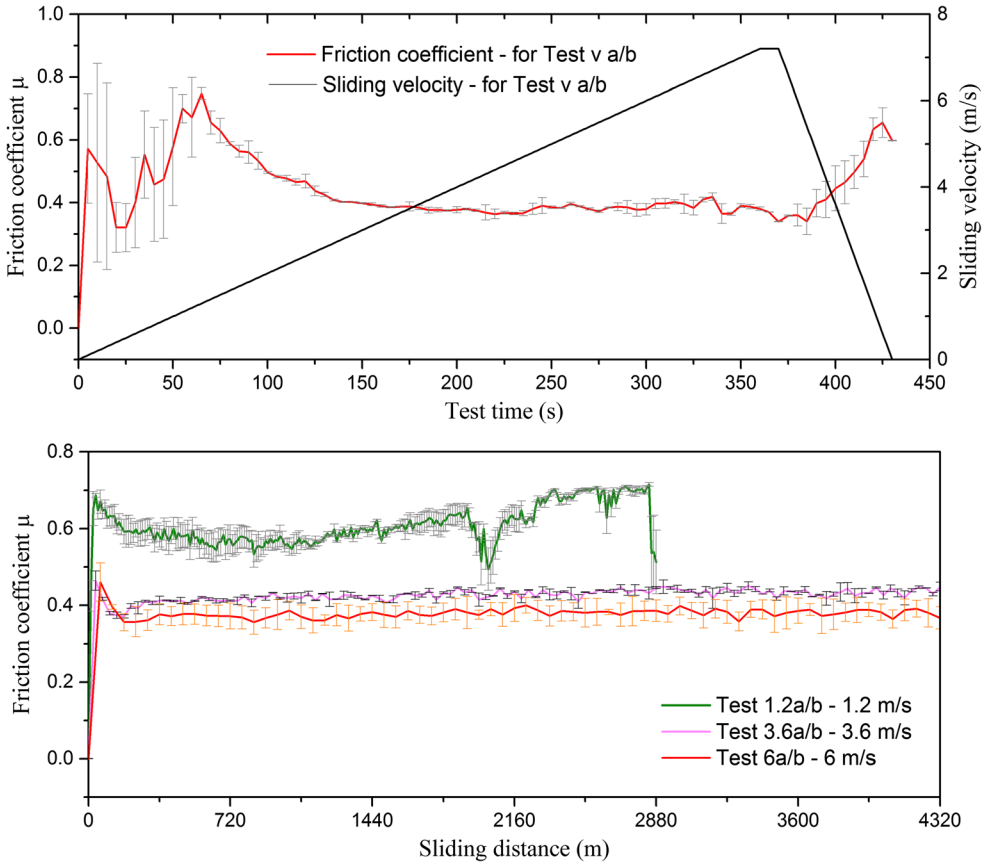

Fig. 4 Friction coefficients averaged of each pair of tests with different sliding velocities (*top*) varying velocity, (*bottom*) constant velocity. The *error bars* show the standard error of the twice repeated tests

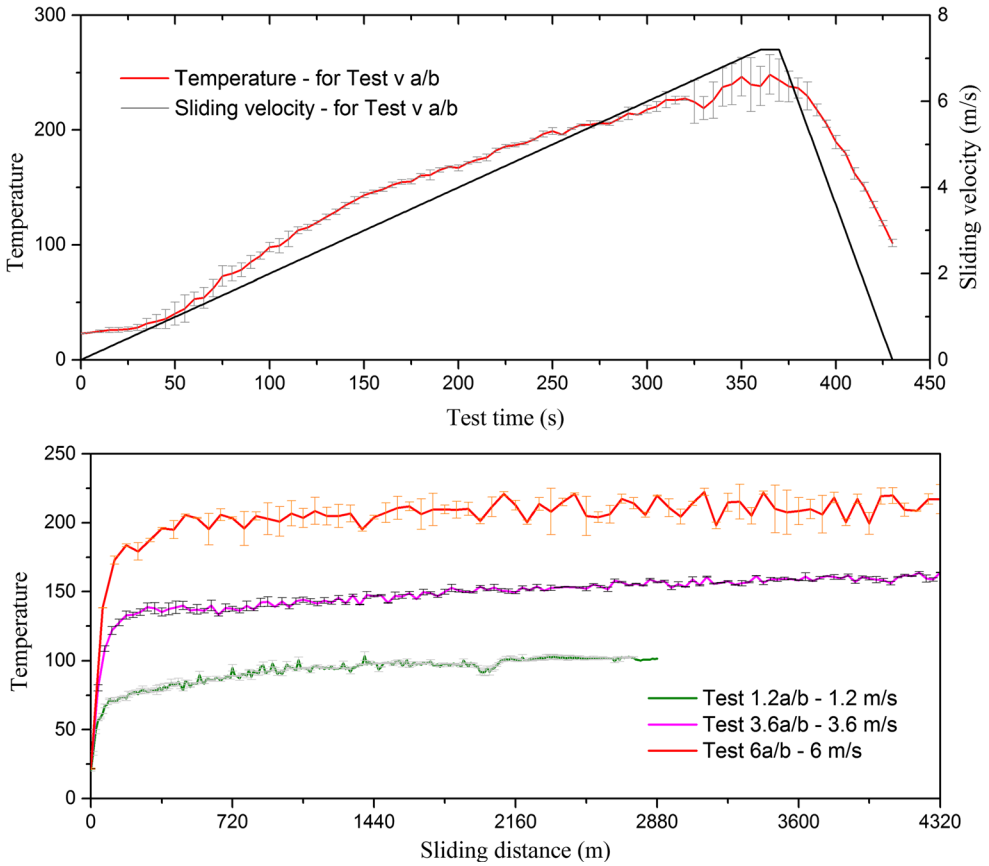

Fig. 5 Temperature (in °C) of contact interfaces that was measured by a thermocouple inserted in a pin specimen with 1 mm from the nominal contact surface. The temperature is averaged of each pair of tests for different sliding velocities, (*top*) varying velocity, (*bottom*) constant velocity. The *error bars* show the standard error of the twice repeated tests

seen that the stable level of friction coefficient on average decreases with increasing velocity. Disregarding running-in periods, the average coefficients are 0.61, 0.43, and 0.38 for the tests with a sliding velocity of 1.2, 3.6, and 6 m/s, respectively.

3.2 Temperature of Friction Interface

The real-time temperatures of the parallel tests are measured, and the result is presented by their average values for each velocity in Fig. 5. It shows clearly a higher temperature for higher velocities for the test of varying velocity. When the velocity increases from 0 to 7.2 m/s, temperature increases continuously over the acceleration period and reaches its peak around 250 °C before it decreases during the deceleration period. For the tests of constant velocities, the temperature increases substantially at the beginning before it reaches a stable level and fluctuates in a small range. It can be seen clearly that the higher the sliding velocity, the greater the average stable value of temperature. Specifically, the average stable temperature measured for the tests with a velocity of 1.2 m/s is about 100 °C, while it increases to 150 °C when the velocity is 3.6 m/s and 210 °C corresponding to 6 m/s.

3.3 Particulate Concentrations and Size Distributions

The total averaged particulate number (PNC) and mass concentrations (PMC) measured by the FMPS and OPS are presented in Fig. 6. The mass concentration is calculated from the number concentration assuming an effective density of 1 g/cm^3 and spherical shaped particles. The effective density is the ratio of the particle mass to the particle volume based on the mobility equivalent diameter [30]. Both the FMPS and OPS levels in number concentration (Fig. 6a) increase with an increase in sliding velocity, and the increase is larger for FMPS compared with OPS. When the velocity is increased from 3.6 to 6 m/s, the number of smaller particles (FMPS result) increases more rapidly than that of larger particles (OPS result). The mass concentration of particles shows an opposite trend for the FMPS and OPS measurements. The mass concentration increases with increasing sliding velocity when measured

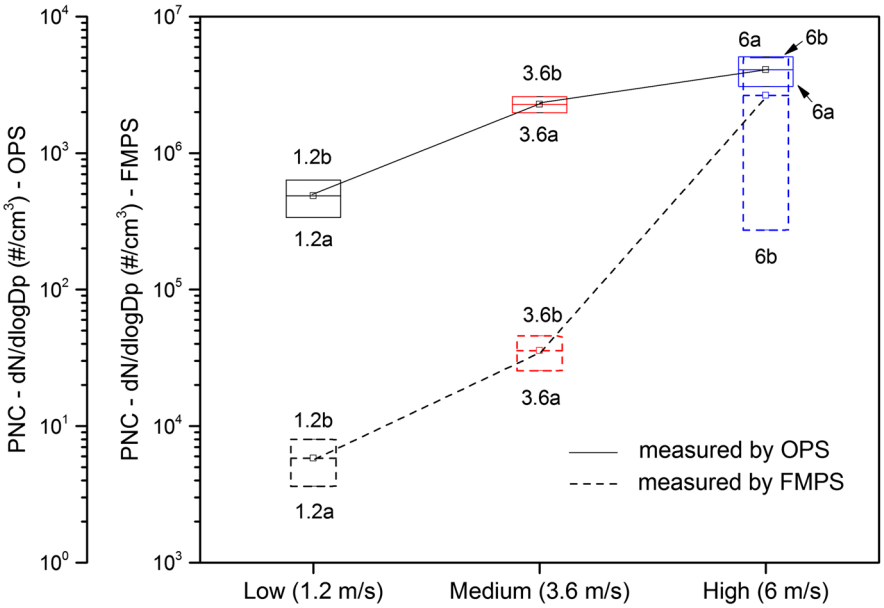

(a) Particulate number concentration

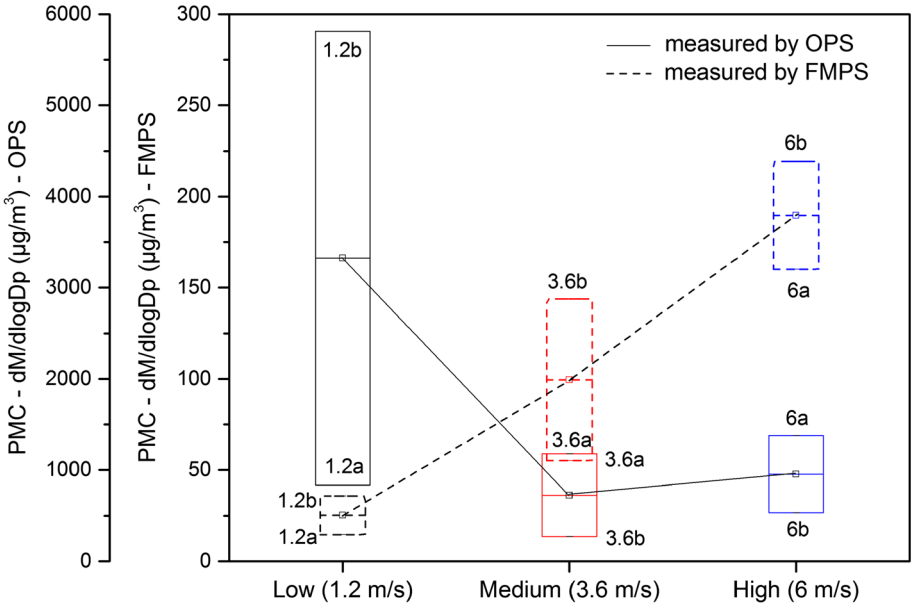

(b) Particulate mass concentration

Fig. 6 Average particulate number concentration (**a**) and mass concentration (**b**) for the tests of different sliding velocities, 1.2a/b, 3.6a/b, and 6a/b marking test 1.2a/b, test 3.6a/b, and test 6a/b. The *box* comprises values of parallel tests (*upper* and *bottom line*). The *line* and the *square* inside the *boxes* represent the mean values

with the FMPS, but decreases for the OPS measurement as shown in Fig. 6b. This strongly indicates a higher number of ultrafine particles for higher sliding velocity.

Figure 7 shows the FMPS result of particulate number concentrations in dependence of the sliding distance, with velocities of 1.2 m/s (test 1.2a and 1.2b), 3.6 m/s (test 3.6a and 3.6b), and 6 m/s (test 6a and 6b). For each velocity, the duplicate tests and their average value are presented. It can be seen that a higher velocity results in greater values of average PNC for small particles (diameter size of 6.04–523 nm). The average PNC is about 6×10^3 particles/cm^3 for 1.2 m/s, 36×10^3 for 3.6 m/s, and 6000×10^3 for 6 m/s. When the velocity is lower (1.2 and 3.6 m/s), the parallel two tests have similar levels of PNC, except a sudden sharp increase in the velocity of 3.6 m/s in test 3.6a. For the higher velocity (6 m/s), the difference for the parallel two tests is significant. Regarding the larger particles (diameter size of 0.3–10 µm) that were measured by the OPS, as presented in Fig. 8, although the average level of PNC increases slightly with increasing sliding velocity, the increase is not as large as for the FMPS measurements. Generally, PNC (all size fractions, but

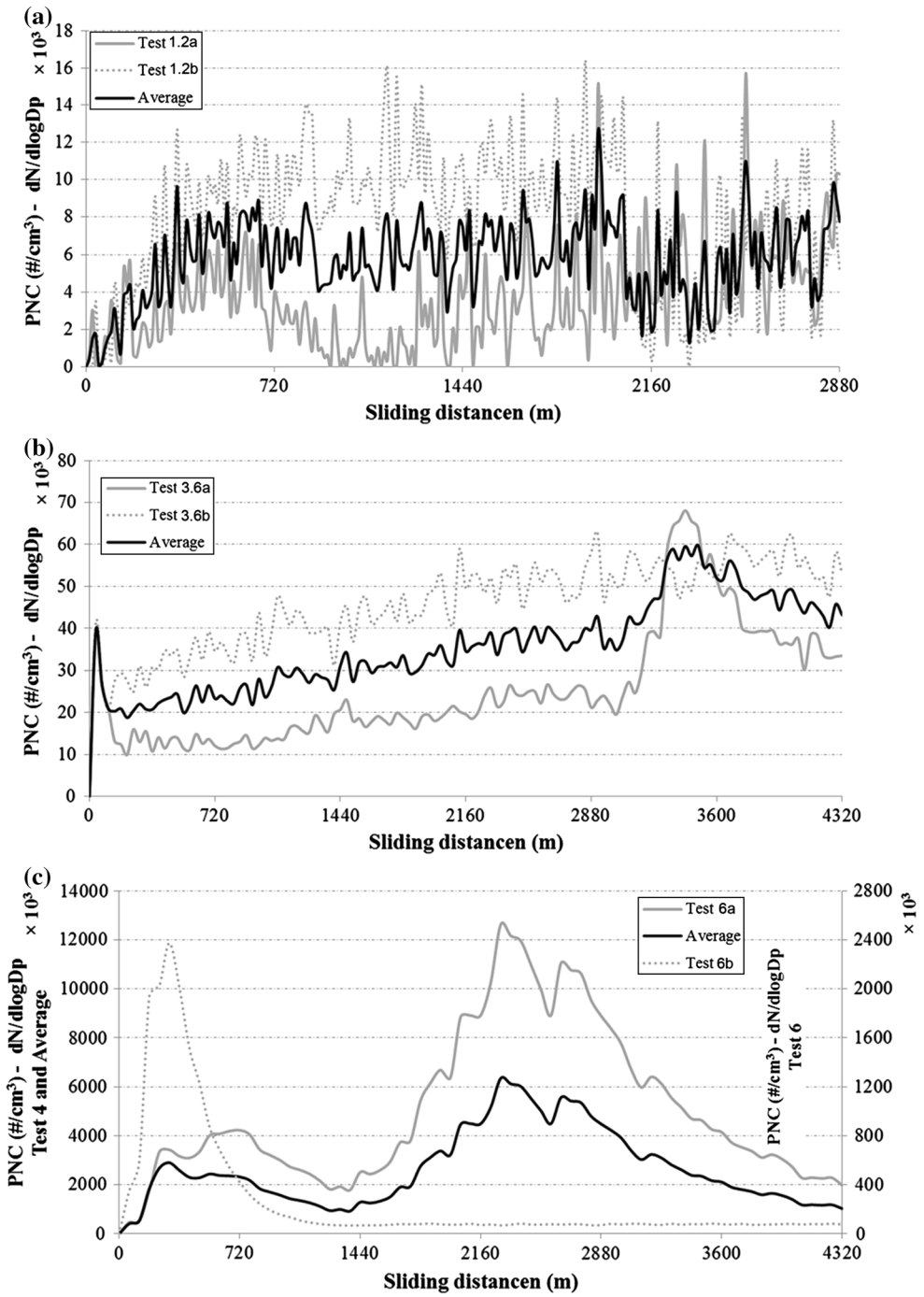

Fig. 7 Particulate number concentrations in dependence of sliding distance that was measured by the FMPS for the tests with sliding velocities of **a** 1.2 m/s, **b** 3.6 m/s, and **c** 6 m/s. For each velocity, the duplicate tests and their average value are presented. Note the different *y*-axis scales

mostly ultrafine particles) increases with increasing velocity.

The normalized particle size distributions in number concentration and mass concentrations for those tests with velocities of 1.2, 3.6, and 6 m/s are shown in Figs. 9 and 10, respectively. The PNC generated with a sliding velocity of 1.2 m/s (test 1.2a and 1.2b) peaks at about 170 nm. This size is the same as for the peaks of test 3.6a and 3.6b, but the levels are lower for 3.6 m/s. In addition, the dominant size range is 70–340 nm for 3.6 m/s, which is wider compared to the tests at 1.2 m/s (around 100–340 nm). When a higher velocity (6 m/s) is applied, the size range shifts towards the ultrafine region of between 6 and 60 nm with a peak at around 10 nm for 6 a and b and an extra

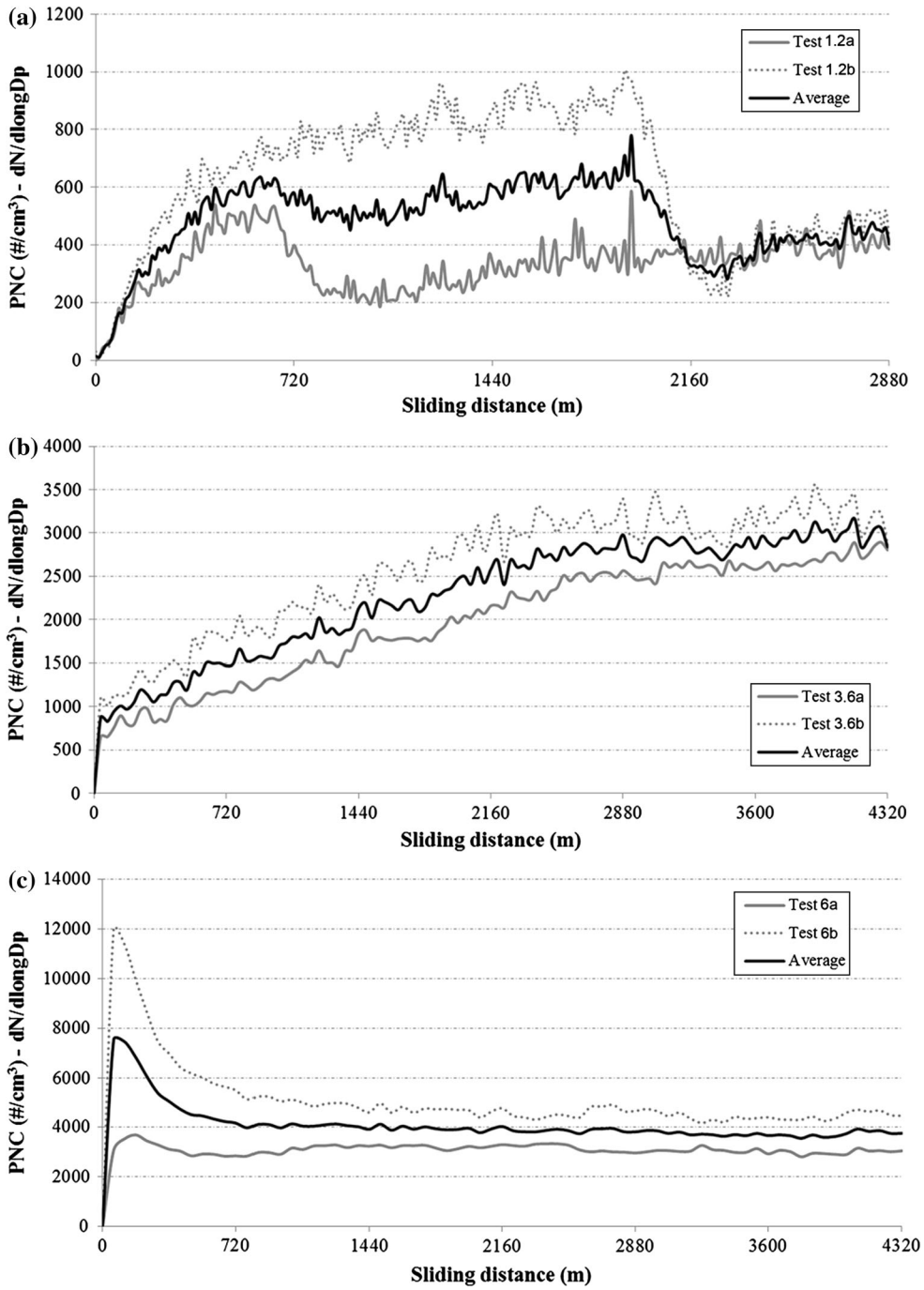

Fig. 8 Particulate number concentrations in dependence of sliding distance that was measured by the OPS for the tests with sliding velocities of **a** 1.2 m/s, **b** 3.6 m/s, and **c** 6 m/s. For each velocity, the duplicate tests and their average value are presented. Note the different *y*-axis scales

peak around 170 nm is observed for test 6b. For the particles that are measured by OPS, a large proportion is occupied by the particles smaller than 0.5 μm for all the tests. Additionally, one peak around 1.7 μm is observed for all the tests and another peak around 0.9 μm is noticeable only for tests 1.2a, 1.2b, and 3.6a. Among those tests, the tests at 1.2 m/s have higher frequencies for the 0.9- and 1.7-mode. With respect to mass concentration (Fig. 10), the dominant mode is around 200–250 nm, while an exceptional mode is around 60 nm for test 6a. When it comes to the OPS result, it varies among those tests, which are all multimodal. The dominant mode for a low velocity is 5.2 μm. It shifts to smaller sizes, and the proportion of large sizes decreases for higher velocities.

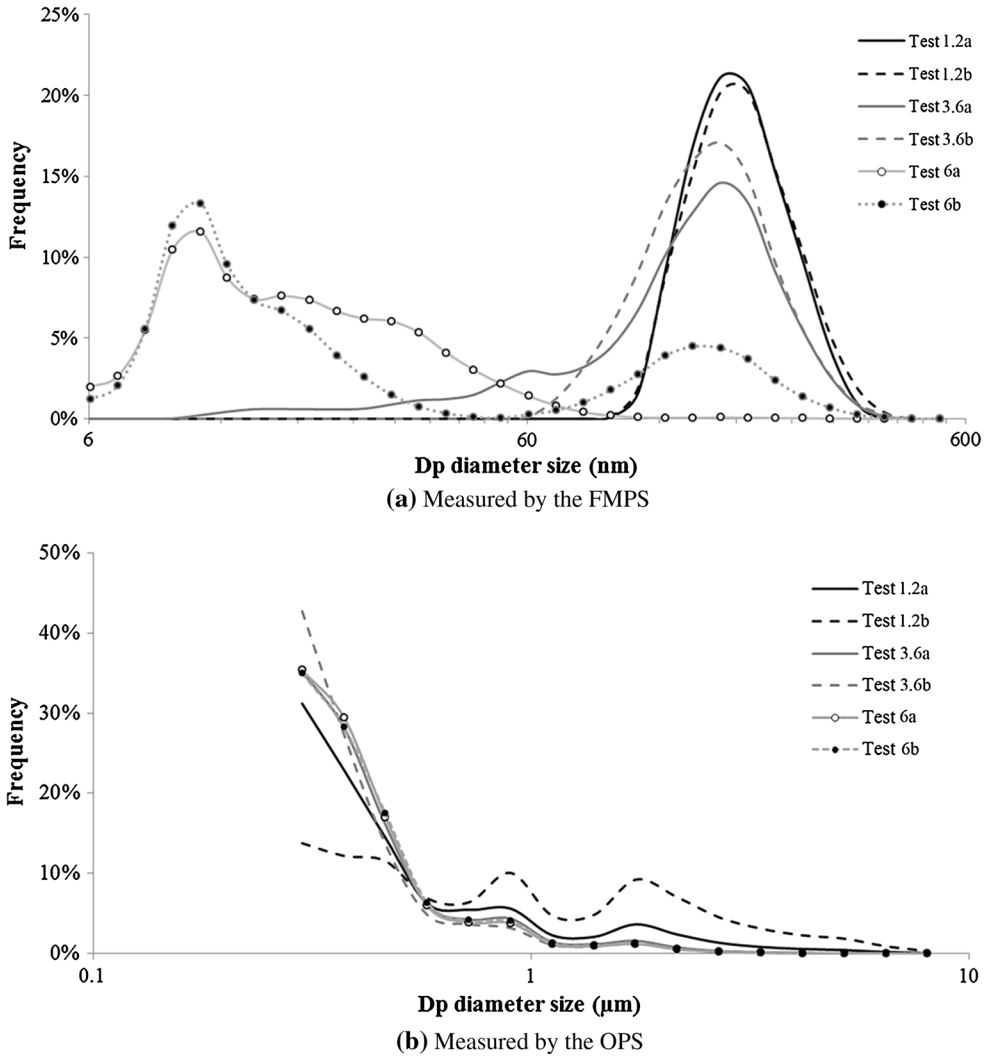

(a) Measured by the FMPS

(b) Measured by the OPS

Fig. 9 Average particle size distribution of PNC under different constant sliding velocities: 1.2 m/s (test 1.2a and 1.2b), 3.6 m/s (test 3.6a and 3.6b), and 6 m/s (test 6a and 6b). **a** Measured by the FMPS, **b** measured by the OPS

3.4 Chemical Compositions

3.4.1 AAS Results

Figure 11 shows the total amount of iron (Fe), copper (Cu), and manganese (Mn) on polycarbonate filters, normalized to sliding distance (2880, 8640, and 14400 m for test 1.2a, test 3.6b, and test 6b, respectively), in dependence of three tests of different sliding velocities and particle size fraction, determined by means of AAS. It should be noted that Fe masses below 1 µg and Mn and Cu masses below 0.1 µg are close to detection limits and need therefore to be interpreted with care. There is a striking effect of the sliding velocity on the Cu content on the filters, as shown in Fig. 11. Test 6b with the highest sliding velocity of 6 m/s shows a significantly larger copper mass on filters, compared to the other tests, between sizes 0.4 and 1.6 µm. The Mn mass on filters depended similarly on the sliding velocities and size fractions compared to the Fe mass: the maximum extent of the Fe and Mn mass on filters seems to be shifted towards smaller particle size fractions for higher sliding velocities. Larger masses are determined for the large size fractions due to their greater mass. Fe is the dominating metal detected. Figure 12 shows the total particle number normalized to the sliding distance. Generally, a higher velocity results in higher number of ultrafine, but a similar or smaller number of larger particles.

3.4.2 Cyclic Voltammetry Measurements

The peak assignments for the cyclic voltammetry measurements are referred to the studies shown in Table 5. The cyclic voltammetry measurements are limited on (1) only electroactive compounds can be detected, and (2) sufficient

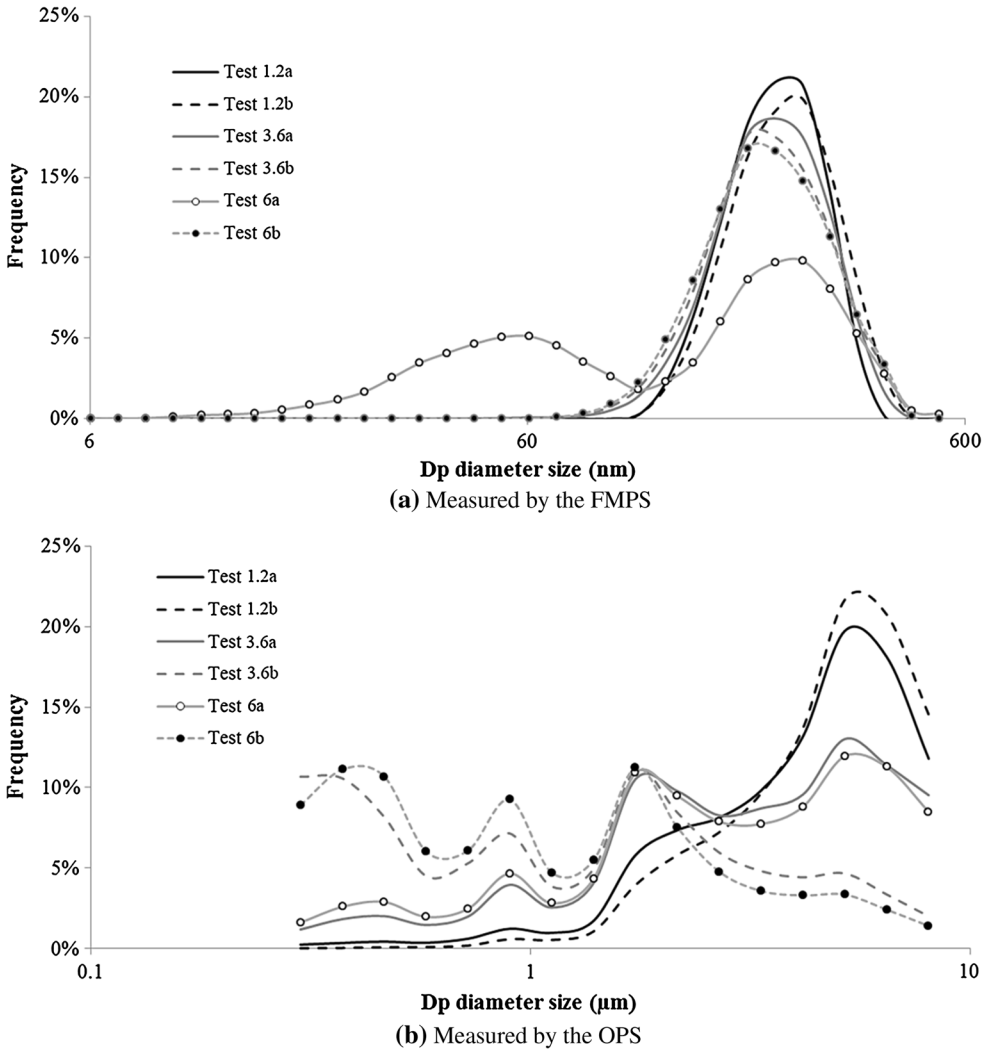

Fig. 10 Average particle size distribution of mass concentration under different constant sliding velocities: 1.2 m/s (test 1.2a and 1.2b), 3.6 m/s (test 3.6a and 3.6b), and 6 m/s (test 6a and 6b). **a** Measured by the FMPS, **b** measured by the OPS

amount of particles must be present on the electrode to detect peaks. The detection limit was found to be sufficiently low, in the range of µg of particle mass in this study. But test 6a (6 m/s), which was run for a shorter time compared to the other tests, was close to detection limits. We analysed size fraction numbers 7, 8, 10, and 11, Table 6, with visible amounts of particles, but even these size fractions were close to detection limits (very small peaks). All of the peak areas are shown in the supplementary file (Table s1). Silicon oxides cannot be detected with this method, as silicon oxides and compounds all are in the tetravalent form and do not have any redox transition within the water stable area.

Three groups of oxides were detected: a Cu corrosion product, neither CuO nor Cu_2O, but probably gerhardite, $Cu_2(OH)_3NO_3$, or a carbonate corrosion product such as malachite, to judge from only one reduction peak close to literature values [35] for these copper compounds, and to judge from the atmospheric conditions and elevated temperature during formation of the Cu compound [36, 37]. The Cu corrosion product was only visible for intermediate size number fractions and certain sliding velocities (it should be noted that the smallest size fractions or the largest size fractions were not measured due to the limit of detection of the electrochemical method). All size fractions tested for test 3.6c (3.6 m/s) and some size fractions (6 and 8) tested for test 1.2b (1.2 m/s) contained the Cu compound. At the velocity of 6 m/s for test 6a and 6c, not much of the Cu compound was observed, but only in small amounts for the larger size fractions. Mn-oxides were present in the trivalent (mostly) or tetravalent form (seldom), but only at small amounts and for some size fractions. The presence of Mn-oxides seemed to be velocity and size dependent, as all samples tested for test 6a (6 m/s) and some fractions for 6c (6 m/s) showed Mn-oxides, especially the small size fractions, but less Mn-oxide was

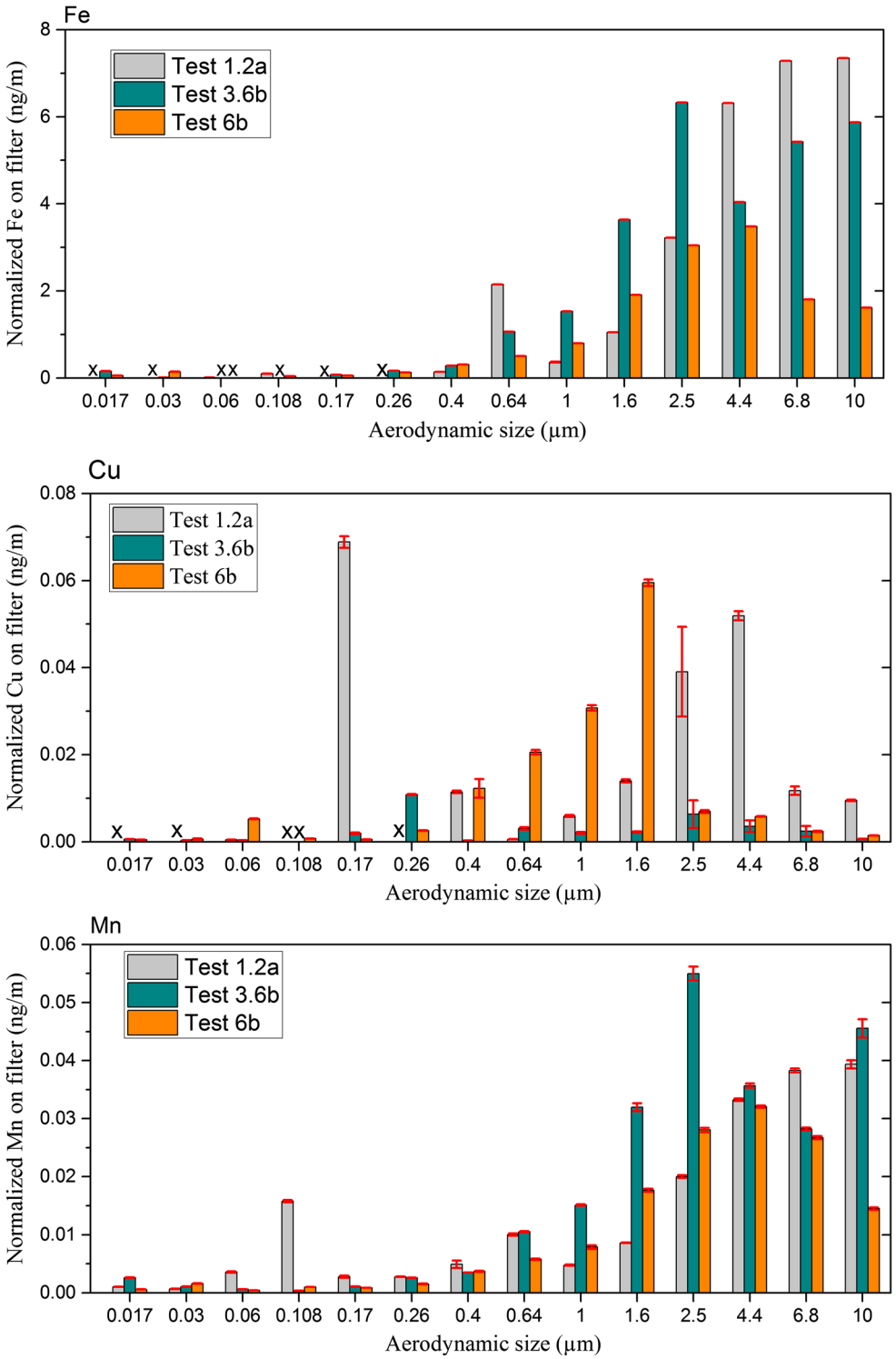

Fig. 11 Total mass of iron (Fe), copper (Cu), and manganese (Mn) on filters normalized to sliding distance (blank values subtracted). The *error bars* show the standard deviation of triplicate readings of the same sample. "*x*" indicates a value smaller than the blank value. Note the different *y*-axis scales

found on test 1.2b (1.2 m/s, only some size fractions) or test 3.6c (3.6 m/s, very small amounts). Fe-oxides were detected on most samples, except one (test 1.2b, number 6), and were mostly assigned to Fe_2O_3, while for the large size fractions of test 6c it seems that the Fe-oxide is mainly Fe_3O_4 or a divalent form [like $Fe(OH)_2$], but not the fully

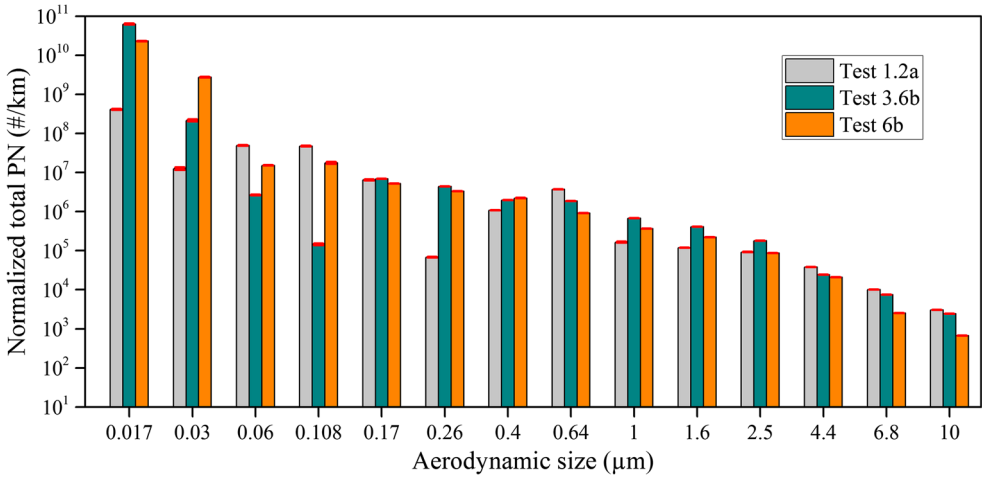

Fig. 12 Total particle number (PN) based on the sum of Fe, Cu, and Mn mass on filters normalized to sliding distance (blank values subtracted). The *error bars* show the standard deviation of triplicate readings of the same sample

Table 5 Peak assignments (all potentials in V versus Ag/AgCl sat. KCl)

Assignment	Reduction peak(s) (V)	Oxidation peak(s) (V)	Reference
Adsorbed oxygen	First reduction after OCP	–	[31]
Fe_2O_3	−1.3	−1.1, −1.0, −0.8	[32, 33]
MnOOH	−0.85, −1.15	−0.5, −0.35, −0.15	[31]
Mn_2O_3 (gamma)	−0.65, −1.15	−0.5, −0.35, −0.15	[31]
MnO_2 (gamma)	−0.4, −0.65, −1.15	−0.5, −0.35, −0.15	[31]
MnO_2 (beta)	−0.75, −1.15	−0.5, −0.35, −0.15	[31]
Mn_3O_4	−1.15	−0.5, −0.35, −0.15	[31]
MnO_2 on stainless steel or in Fe_2O_3	−0.6	−0.2	[32]
CuO	−0.5, −0.7 (extrapolated to pH 13)	−0.5, −0.3	[34]
Different copper corrosion products	−0.9, −1.0 (extrapolated to pH 13)	Not reported	[35]

oxidized Fe_2O_3. Oxidation tests indicated that Fe_3O_4 could also be present for test 1.2b, number 10, and test 6c, number 9 and 12. Oxidation tests performed for test 3.6c indicated a small oxidation peak, but this seemed rather to correlate to dissolution of the copper compound, which in those tests was not visible anymore in subsequent reduction and oxidation cycles. No oxidation test was performed for test 6a (6 m/s) due to the low amount of particles collected.

3.4.3 SEM/EDS Chemical Results

SEM/EDS measurements confirmed the main elements Fe, Si, and Mn, see Table 7. Mn was only detected for test 6a (6 m/s), number 12, and for test 3.6a (3.6 m/s) for some spots, but not for test 1.2b, in accordance with the cyclic voltammetry results (more Mn-oxides for higher sliding velocity and smaller size fractions). One size fraction (number 6) of test 6a did not show any metal particles, but contamination particles (Ca-rich).

4 Discussion

In this study, the frictional processes and particle emissions of a third rail and shoe during sliding contact are simulated using a constant average pressure and different sliding velocities. With an increasing velocity, the normalized wear rate per unit sliding distance (µg/m) decreases. The wear rate is significantly higher for a low velocity compared with others but similar levels when the velocity reaches certain values (3.6 and 6 m/s). In test 6b, it is negative for the disc and is not shown in the result. It means that the mass of material built up on the disc surface is greater than that removed. One explanation to this is that a large region of the surface has been oxidized to form a third-body layer and a certain amount of particles is adhered to the worn surface in pits (Fig. 13c) that cannot be cleaned by ultrasound cleaning. The third-body layer could be a sink for released particles to form a larger contact area, which will result in a lower contact pressure and therefore a lower wear rate of the material. It means

Table 6 Assignments of all peaks in the cyclic voltammetry measurements

Test	Particle size filter number	Cyclic voltammetry measurements	Peak assignments (all potentials in V versus Ag/AgCl sat. KCl)
Test 1.2b (1.2 m/s)	6	Reduction → oxidation	copper compound (such as gerhardite), very small amounts of MnOOH or Mn_3O_4 possible
Test 1.2b (1.2 m/s)	8	Reduction → oxidation	Fe_2O_3, amounts of MnO_2 or Mn_2O_3 possible, copper compound (such as gerhardite) possible
Test 1.2b (1.2 m/s)	10	Reduction → oxidation	Fe_2O_3, some Fe_3O_4 or divalent Fe (to judge from oxidation of number 11)
Test 1.2b (1.2 m/s)	11	Oxidation → reduction	Confirms that divalent Fe or Fe_3O_4 is partially present in test 1.2b, number 10
Test 3.6c (3.6 m/s)	4	Oxidation → reduction	oxidation peak possibly due to dissolution of Cu compound
Test 3.6c (3.6 m/s)	5	Reduction → oxidation	Probably Fe_2O_3, other di- or trivalent Fe possible, copper compound (such as gerhardite), very small amounts of MnOOH or Mn_3O_4 possible
Test 3.6c (3.6 m/s)	7	Reduction → oxidation	Copper compound (such as gerhardite), di- or trivalent Fe, very small amounts of Mn_3O_4 and/or MnOOH possible
Test 3.6c (3.6 m/s)	10	Oxidation → reduction	oxidation peak possibly due to dissolution of Cu compound
Test 3.6c (3.6 m/s)	11	Reduction → oxidation	Fe_2O_3, copper compound (such as gerhardite), very small amounts of amounts of Mn_3O_4 and/or MnOOH possible
Test 6a (6 m/s)	7	Reduction → oxidation	amounts of MnO_2 or Mn_2O_3 possible (close to detection limit)
Test 6a (6 m/s)	8	Reduction → oxidation	amounts of MnO_2 or Mn_2O_3 possible (close to detection limit)
Test 6a (6 m/s)	10	Reduction → oxidation	di- or trivalent Fe, MnOOH or Mn_3O_4
Test 6a (6 m/s)	11	Reduction → oxidation	MnO_2 or Mn_2O_3, small amounts of di- or trivalent Fe
Test 6c (6 m/s)	4	Reduction → oxidation	MnO_2, MnOOH or Mn_3O_4, small amounts of Mn_2O_3 possible, small amounts of di- or trivalent Fe
Test 6c (6 m/s)	5	Oxidation → reduction	Confirmation that only a small part of Mn- or Fe-oxide in test 6c, number 4 was not fully oxidized.
Test 6c (6 m/s)	9	Oxidation → reduction	A minor part of Fe-oxide in test 6c, number 10 is not fully oxidized, but in the divalent form or Fe_3O_4
Test 6c (6 m/s)	10	Reduction → oxidation	Fe_2O_3, Fe_3O_4, or divalent Fe-oxide, small amounts of copper compound (such as gerhardite)
Test 6c (6 m/s)	11	Reduction → oxidation	Fe_3O_4 or divalent Fe-oxide, Fe_2O_3 possible, small amount of copper compound (such as gerhardite), very small amounts of MnOOH or Mn_3O_4 possible
Test 6c (6 m/s)	12	Oxidation → reduction	A major part of the Fe-oxide in test 6c, number 11, is not fully oxidized and hence in the divalent form or Fe_3O_4

that the amount of released particles would be reduced, but does not mean any decrease in the particle number. In fact, the number of released particles is higher at higher velocity due to the high amount of ultrafine particles that are generated. For the tests at 1.2 m/s, a much higher friction coefficient is observed compared to the tests at higher velocities. Coefficient of friction decreases from 0.61 to 0.41 as temperature increases from 100 to 210 °C with the velocity increased from 1.2 to 6 m/s. This supports the result from previous study that the wear rate and friction coefficient are typically observed to decrease remarkably over a relatively narrow range of temperature [18]. One can attribute this to different features of oxide layers formulated in the interfaces which act as third-body layers to influence the coefficient of friction. According to the BSE graphs in Fig. 13, the oxidative degree increases with increasing velocity, as is indicated by the darker area and would be expected from the higher temperature [38, 39]. BSE graphs show atomic density, and the presence of oxygen for the darker region on the image indicates an oxide layer, confirmed by a larger percentage of oxygen measured by EDS (data not shown). At higher temperature,

Table 7 Detected elements by means of SEM/EDS[a] (wt%)

Test number	Filter number	Spot number	Elements							
			Fe	Mn	Si	Al	Ca	S	Na	Mg
Test 1.2b (1.2 m/s)	14	Spot 1	97.9		1.2	0.4				0.5
		Spot 3	99.1		0.9					
		Spot 4	86.5		5.3	1.0	1.8	2.2	1.6	1.5
		Spot 5	99.6		0.4					
		Spot 6	94.3		4.3			1.4		
Test 3.6a (3.6 m/)	10	Spot 1	85.3		3.6			5.7	5.3	
		Spot 3	95.6		3.1			1.3		
		Spot 4	96.9	0.9	2.2					
		Spot 5	95.9	0.9	2.7			0.6		
Test 6a (6 m/s)	12	Spot 1	89.7	2.0	4.3			4.0		
		Spot 3	91.5		3.5			3.0	2.0	
		Spot 4	95.3	1.2	3.6					
		Spot 5	94.9	0.9	3.5			0.6		
	6	Spot 1			2.9		84.8	7.9	4.4	
		Spot 3			0.8		98.3	0.9		
		Spot 4			5.2		66.3	20.6	7.9	

[a] This instrument cannot detect light elements such as O, N, and C. The information depth is μm, which means that this technique is not surface sensitive

the surfaces develop thicker oxide layers and the formation of a large number of patches that are attached (as examples shown in Fig. 13) would support the bearing load and eventually protect the surfaces from wear. In addition, the retention of wear particles within scars and around patches leads to the formation of a relatively smooth bearing bed to reduce wear. The increasing amount of ultrafine particles at higher temperature would be another reason for the drop in wear rate, since ultrafine particles are easily be sintered on the wear surface to form wear protective tribofilms [21, 22]. Iron oxides have been detected for most wear particles on filters, and they are mostly assigned to Fe_2O_3, but also iron oxides of lower oxidation state for test 6c. More manganese oxides present for small particles would also protect the surface from wear, since those oxides would be relatively hard and the particles are small to be easily sintered on the surface.

A larger oxide thickness for higher velocity and the presence of cracks indicate that a mild oxidative wear regime persists at medium and high velocity in which only part of the oxidative layer is removed. In contrast, the flake-shape particles observed for the low velocity test (1.2 m/s) together with the oxide layer analysis suggest a severe oxidative wear mechanism in which the whole oxide layer and potentially also the bulk material is removed. It is also demonstrated when we combine the results of AAS, CV measurements, and particle size distribution that the released particles at low velocity are in larger sizes due to severe wear, which would usually increase the wear rate of the contact [22]. This is different for tests at high velocity. When the velocity is high, particles that are released from the outer oxide layer were shown to be of more ultrafine fractions. Those ultrafine oxide particles are easily sintered on the wear surface thereby inducing transition to mild wear [21]. The wear rate of the contact is hence reduced. However, a limitation of this work is the lack of electric current flowing through the specimen. That has been shown to have significant effect on the contact temperature and on the wear mechanisms of the frictional pairs [13, 27, 28]. When sliding along the third rail, the shoe vibrates and moves in and out of contact. Those vibrations could affect arc discharges and consequently the wear mechanisms [15]. However, these cannot be observed in this study by a scaled simulation set-up, where the sliding contact is continuous and stable.

As indicated by the particle counter measurements and AAS results, an increasing amount of ultrafine particles are formed at high velocity, whilst larger particles become dominant at low velocity which increase the wear rates of the contacts. Oxide layers at elevated temperature for higher sliding velocity would account for the increase of small particles, since oxides are much harder and more brittle. The Vickers hardness of oxide scales on iron as shown in [40] is 6.7 GPa for Fe_2O_3, 4 GPa for Fe_3O_4, and 3.5 GPa for FeO. Those values are greater than the hardness of the disc bulk material which is 1.15 GPa. With a constant sliding velocity, the particle number concentration tends to be stable after the running-in period, except that some sudden increases of fine particles observed such as in tests 3.6a, 6a, and 6b. One explanation for those suddenly

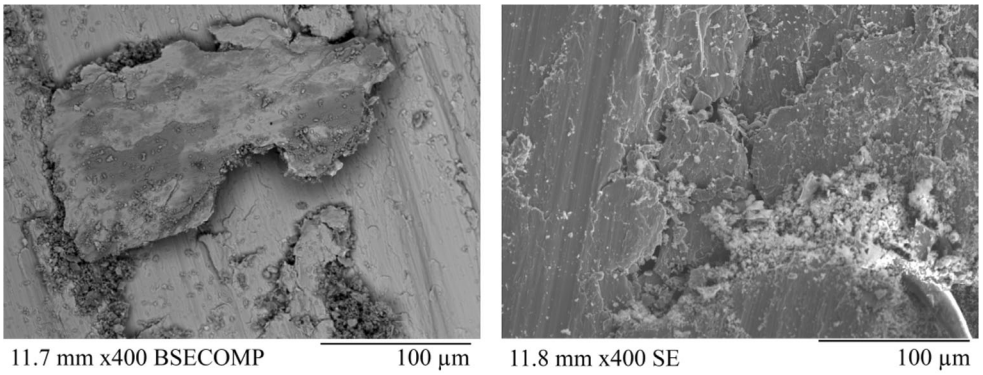

(a) Test 1.2a – sliding velocity of 1.2 m/s

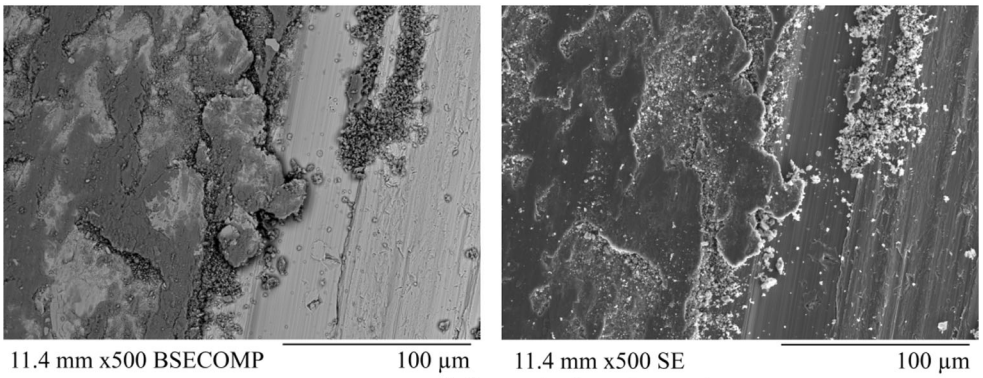

(b) Test 3.6a – sliding velocity of 3.6 m/s

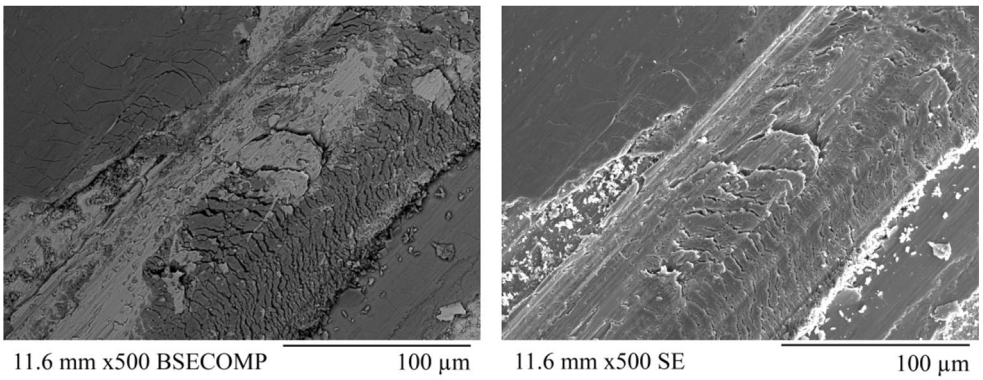

(c) Test 6b – sliding velocity of 6 m/s

Fig. 13 Backscattered electron SEM images (*left*) and secondary electron SEM images (*right*) of worn disc surfaces under different sliding speed conditions, test 1.2a (1.2 m/s), test 3.6a (3.6 m/s), and test 6b (6 m/s). The BSE images show atomic density, indicating an oxide layer by showing a darker region combining with EDS result. Larger oxide area is for the test at higher velocity. Note that the top two pictures do not show the same position. **a** Test 1.2a—sliding velocity of 1.2 m/s, **b** test 3.6a—sliding velocity of 3.6 m/s, **c** test 6b—sliding velocity of 6 m/s

sharp increases could be the collapse of particle plateaus that are formulated during the friction process, which leads to the release of a large amount of blocked particles.

The main elements contained in the wear particles are Fe, silicon (Si), Mn, and Cu. Since cyclic voltammetry cannot detect any Si species, it cannot be judged whether Si is present in the surface oxide and/or as dust or surface contamination. However, since Si has a high oxygen affinity, it is likely to be present in the surface oxide [41]. The dominant size fraction of the particles (in mass) was sliding velocity dependent, that is, the higher sliding velocity, the smaller size the particle. It is supported by the AAS measurements that a higher number of smaller particles are seen for higher velocities. Both the AAS result and the cyclic voltammetry measurement confirm that much more Fe-oxides are shown for large particles. As concluded from the result of cyclic voltammetry measurements, the surface oxide of the iron-containing wear

particles mostly contained iron oxides, mostly assigned to Fe_2O_3. Fe_3O_4 or divalent form [like $Fe(OH)_2$] would be shown in the tests with a high velocity. In agreement with studies on gas-atomized stainless steel particles [42, 43], manganese oxides are present in the surface oxide, to a much larger extent as expected from their bulk composition, and increasingly with decreasing particle size and possibly increasing sliding velocity. This is explained by the higher cooling rate for smaller particles and the large oxygen affinity of manganese [42, 44]. The Cu compound was detected in the surface oxide for some samples by cyclic voltammetry, especially for the tests at 3.6 m/s, and more Cu was observed in the particle mass for the highest velocity, 6 m/s, by means of AAS. If the inconsistent result is dependent on more than random, it might be some experimental uncontrolled conditions such as relative humidity, or Cu present in some of the particles for the highest velocity (determined by AAS), but not in their outermost surface oxide (determined by CV). We speculate that the observed copper compound is gerhardite, $Cu(OH)_3NO_3$, formed at elevated temperature in air [37]. Its sporadic formation may be due to the fact that Cu is a minor alloying element in the materials investigated, not present on the surface, and that the necessary environmental conditions for its formation (temperature and atmosphere) may only be available occasionally.

5 Conclusions

Particles that are released from third rail-to-shoe sliding contact are an important contributor to PM levels in the metro environment. In this study, a series of pin-on-disc tests have been carried out to simulate the frictional behaviour of rail–shoe dry sliding. The wear, wear particles, and temperature were investigated in dependence of the wear particle size and sliding velocities. The pin-on-disc test set-up simulates constant conditions in terms of average contact pressure and sliding contact. It differs from the rail/shoe contact in terms of impact loading when the shoe enters that contact and also for accelerating and decelerating traffic conditions. However, this test set-up provides a possibility to study how specific running conditions affect the particle emissions and these kinds of results may in the future be used to map for instance the source content from the third-rail contact in field studies. Further studies are necessary to scale these results to the actual third-rail contact. The following main conclusions can be drawn from this study additionally:

1. An increasing sliding velocity results in higher concentration of ultrafine particles.
2. The dominant wear mechanism depends on the sliding velocity. Mild oxidative wear persists at the higher sliding velocities and a severe oxidative wear regime can be identified at the lower sliding velocity.
3. The ratio of manganese to iron surface oxides strongly increases with decreasing particle size.
4. Significantly more Mn-oxides are present for small particles and significantly more Fe-oxides for large particles.
5. A copper compound forms sporadically, probably gerhardite.

References

1. Bigert, C., Alderling, M., Svartengren, M., Plato, N., de Faire, U., Gustavsson, P.: Blood markers of inflammation and coagulation and exposure to airborne particles in employees in the Stockholm underground. Occup. Environ. Med. **65**, 655–658 (2008)
2. Cartenì, A., Cascetta, F., Campana, S.: Underground and ground-level particulate matter concentrations in an Italian metro system. Atmos. Environ. **101**, 328–337 (2015)
3. Querol, X., Moreno, T., Karanasiou, A., Reche, C., Alastuey, A., Viana, M., Font, O., Gil, J., de Miguel, E., Capdevila, M.: Variability of levels and composition of PM_{10} and $PM_{2.5}$ in the Barcelona metro system. Atmos. Chem. Phys. **12**, 5055–5076 (2012)
4. Kam, W., Cheung, K., Daher, N., Sioutas, C.: Particulate matter (PM) concentrations in underground and ground-level rail systems of the Los Angeles Metro. Atmos. Environ. **45**, 1506–1516 (2011)
5. Park, D.-U., Ha, K.-C.: Characteristics of PM10, PM2.5, CO_2 and CO monitored in interiors and platforms of subway train in Seoul, Korea. Environ. Int. **34**, 629–634 (2008)
6. Braňĭ, M.: The contribution of ambient sources to particulate pollution in spaces and trains of the Prague underground transport system. Atmos. Environ. **40**, 348–356 (2006)
7. Gustafsson, M., Blomqvist, G., Swietlicki, E., Dahl, A., Gudmundsson, A.: Inhalable railroad particles at ground level and subterranean stations—physical and chemical properties and relation to train traffic. Transp. Res. Part D Transp. Environ. **17**, 277–285 (2012)
8. Midander, K., Elihn, K., Wallén, A., Belova, L., Karlsson, A.-K.B., Wallinder, I.O.: Characterisation of nano- and micron-sized airborne and collected subway particles, a multi-analytical approach. Sci. Total Environ. **427–428**, 390–400 (2012)
9. Kain, J., Karlsson, H.L., Möller, L.: DNA damage induced by micro- and nanoparticles—interaction with FPG influences the detection of DNA oxidation in the comet assay. Mutagenesis **27**, 491–500 (2012)
10. Karlsson, H.L., Holgersson, Å., Möller, L.: Mechanisms related to the genotoxicity of particles in the subway and from other sources. Chem. Res. Toxicol. **21**, 726–731 (2008)

11. Loxham, M., Cooper, M.J., Gerlofs-Nijland, M.E., Cassee, F.R., Davies, D.E., Palmer, M.R., Teagle, D.A.H.: Physicochemical characterization of airborne particulate matter at a mainline underground railway station. Environ. Sci. Technol. **47**, 3614–3622 (2013)
12. Kang, S., Hwang, H., Park, Y., Kim, H., Ro, C.-U.: Chemical compositions of subway particles in Seoul, Korea determined by a quantitative single particle analysis. Environ. Sci. Technol. **42**, 9051–9057 (2008)
13. Dong, L., Chen, G.X., Zhu, M.H., Zhou, Z.R.: Wear mechanism of aluminum-stainless steel composite conductor rail sliding against collector shoe with electric current. Wear **263**, 598–603 (2007)
14. Dong, L., Zhong, W., Chen, G.X., Lewis, R.: Effects of polarity on the friction and wear of collector shoes deployed in a metro traction system. Proc. Inst. Mech. Eng. Part F J. Rail Rapid Transit. **228**, 323–330 (2013)
15. Yang, H., Chen, G., Zhang, S., Zhang, W.: Effect of the vibration on friction and wear behavior between the carbon strip and copper contact wire pair. Proc. Inst. Mech. Eng. Part J J. Eng. Tribol. **226**, 722–728 (2012)
16. Quinn, T.F.J.: The oxidational wear of low alloy steels. Tribol. Int. **35**, 691–715 (2002)
17. Sundh, J., Olofsson, U.: Relating contact temperature and wear transitions in a wheel–rail contact. Wear **271**, 78–85 (2011)
18. Pearson, S.R., Shipway, P.H., Abere, J.O., Hewitt, R.A.A.: The effect of temperature on wear and friction of a high strength steel in fretting. Wear **303**, 622–631 (2013)
19. Clark, W.T., Pritchard, C., Midgley, J.W.: Mild wear of unlubricated hard steels in air and carbon dioxide. In: Proceedings of the Institution of Mechanical Engineeris, pp. 97–105 (1967)
20. Mishra, A.: Introduction to wear. Createspace Independent Publishing Platform, United States (2015)
21. Kato, H., Komai, K.: Tribofilm formation and mild wear by tribosintering of nanometer-sized oxide particles on rubbing steel surfaces. Wear **262**, 36–41 (2007)
22. Kato, H.: Effects of supply of fine oxide particles onto rubbing steel surfaces on severe-mild wear transition and oxide film formation. Tribol. Int. **41**, 735–742 (2008)
23. Kukutschová, J., Moravec, P., Tomášek, V., Matějka, V., Smolík, J., Schwarz, J., Seidlerová, J., Safářová, K., Filip, P.: On airborne nano/micro-sized wear particles released from low-metallic automotive brakes. Environ. Pollut. **159**, 998–1006 (2011)
24. Olofsson, U.: A study of airborne wear particles generated from the train traffic—block braking simulation in a pin-on-disc machine. Wear **271**, 86–91 (2011)
25. Olofsson, U., Olander, L.: On the identification of wear modes and transitions using airborne wear particles. Tribol. Int. **59**, 104–113 (2013)
26. Olofsson, U., Olander, L., Jansson, A.: A study of airborne wear particles generated from a sliding contact. J. Tribol. **131**, 044503 (2009)
27. Ding, T., Chen, G.X., Bu, J., Zhang, W.H.: Effect of temperature and arc discharge on friction and wear behaviours of carbon strip/copper contact wire in pantograph–catenary systems. Wear **271**, 1629–1636 (2011)
28. Dong, L., Lewis, R., Li, C.X., Zhu, W.B., Wang, H.S.: Finite element assessment of the temperature field couple under joule heat and friction heat between a third rail and collector shoe. Proc. Inst. Mech. Eng. Part J J. Eng. Tribol. **229**, 1086–1094 (2015)
29. Schunk Group: Third-rail-systems from Schunk: the newest design of current collectors for the third rail. http://www.schunk-benelux.nl/sixcms/media.php/1702/17_04_engl.pdf
30. McMurry, P.H., Wang, X., Park, K., Ehara, K.: The relationship between mass and mobility for atmospheric particles: a new technique for measuring particle density. Aerosol Sci. Technol. **36**, 227–238 (2002)
31. Chouaib, F., Cauquil, O., Lamache, M.: Comportement electrochimiue d' oxydes de manganese, en milieu alcalin. Electrochim. Acta **26**, 325–328 (1980)
32. Linhardt, P.: Electrochemical identification of higher oxides of manganese in corrosion relevant deposits formed by microorganisms. Mater. Sci. Forum **289**, 1267–1274 (1998)
33. Neugebauer, H., Nauer, G., Brinda-Konopik, N., Gidaly, G.: The in situ determination of oxidation products on iron electrodes in alkaline electrolytes using multiple internal reflection fourier transform infrared spectroscopy. J. Electroanal. Chem. **122**, 381–385 (1981)
34. Hedberg, Y.S., Pradhan, S., Cappellini, F., Karlsson, M.-E., Blomberg, E., Karlsson, H.L., Odnevall Wallinder, I., Hedberg, J.F.: Electrochemical surface oxide characterization of differently toxic metal nanoparticles (Mn, Cu and Al) and the relation to toxicity. Electrochim. Acta **212**, 360–371 (2016)
35. Malvault, J.Y., Lopitaux, J., Delahaye, D., Lenglet, M.: Cathodic reduction and infrared reflectance spectroscopy of basic copper(II) salts on copper substrate. J. Appl. Electrochem. **25**, 841–845 (1995)
36. Kannan, S., Rives, V., Knözinger, H.: High-temperature transformations of Cu-rich hydrotalcites. J. Solid State Chem. **177**, 319–331 (2004)
37. Aastrup, T., Wadsak, M., Leygraf, C., Schreiner, M.: In situ studies of the initial atmospheric corrosion of copper influence of humidity, sulfur dioxide, ozone, and nitrogen dioxide. J. Electrochem. Soc. **147**, 2543 (2000)
38. Bertrand, N., Desgranges, C., Poquillon, D., Lafont, M.C., Monceau, D.: Iron oxidation at low temperature (260–500 °C) in air and the effect of water vapor. Oxid. Met. **73**, 139–162 (2010)
39. Chen, R.Y., Yuen, W.Y.D.: Review of the high-temperature oxidation of iron and carbon steels in air or oxygen. Oxid. Met. **59**, 433–468 (2003)
40. Takeda, M., Onishi, T., Nakakubo, S., Fujimoto, S.: Physical properties of iron-oxide scales on si-containing steels at high temperature. Mater. Trans. **50**, 2242–2246 (2009)
41. Hryha, E., Gierl, C., Nyborg, L., Danninger, H., Dudrova, E.: Surface composition of the steel powders pre-alloyed with manganese. Appl. Surf. Sci. **256**, 3946–3961 (2010)
42. Hedberg, Y., Norell, M., Hedberg, J., Szakalos, P., Linhardt, P., Odnevall Wallinder, I.: Surface characterisation of fine inert gas and water atomised stainless steel 316L powders: formation of thermodynamically unstable surface oxide phases. Powder Metall. **56**, 158–163 (2013)
43. Hedberg, Y., Midander, K.: Size matters: mechanism of metal release from 316L stainless steel particles is governed by size-dependent properties of the surface oxide. Mater. Lett. **122**, 223–226 (2014)
44. Hedberg, Y., Norell, M., Linhardt, P., Bergqvist, H., Odnevall Wallinder, I.: Influence of surface oxide characteristics and speciation on corrosion, electrochemical properties and metal release of atomized 316L stainless steel powders. Int. J. Electrochem. Sci. **7**, 11655–11677 (2012)